J. Fluid Mech. (1975), *vol.* 68, *part* 1, *pp.* 157–175
Printed in Great Britain

Stability analysis of rotational Couette flow of stratified fluids

By E. M. WITHJACK† AND C. F. CHEN
Mechanical, Industrial and Aerospace Engineering Department,
Rutgers University, New Brunswick, New Jersey 08903

(Received 16 May 1974)

A linear stability analysis is used to investigate the stability of rotational Couette flow of stratified fluids. The linearized time-dependent perturbation equations are solved using explicit finite-difference approximations. Small random axisymmetric perturbations of a given wavelength are initially distributed in the flow field, and their development in time is obtained by numerical integration. It is found that the kinetic energy of the perturbations oscillates in time owing to the periodic transformation of the disturbance flow field from a one-vortex system to a two-vortex system and vice versa. The neutral condition is defined as the state in which the maxima of the perturbation kinetic energy curve no longer change in time. A neutral-stability curve is obtained using the experimentally observed critical wavelengths. It is in general agreement with the experimental data, and it confirms the experimental result that stable density stratification enhances stability.

1. Introduction

The results of an experimental investigation of the stability of rotational Couette flow of stably stratified fluids have been presented by Withjack & Chen (1974, hereafter referred to as I). They reported that the onset of instability is inhibited by a stable density gradient, and by using shadowgraph and dye-trace methods observed a rather complex vortex pattern at the critical conditions. For cylinders rotating in the same direction, instabilities appeared in the critical state as a spiral wave form, which itself was not very stable. With counter-rotating cylinders, the instabilities appeared as regularly spaced vortices which, for the most part, were neither symmetrical Taylor vortices nor simple spirals. In this paper, we present the results of a stability analysis of Couette flow with a stabilizing density gradient.

The stability of homogeneous fluids in rotational Couette flow has been the subject of extensive theoretical investigation. Most widely treated have been cases with either a small gap or speed ratios μ (the ratio of the angular speed Ω_2 of the outer cylinder to that of the inner cylinder Ω_1) which are close to zero. When the gap is large and the speed ratio $\mu < -0{\cdot}5$, mathematical solutions of the eigenvalue problem become more difficult to obtain. The narrow-gap problem

† Present address: Transportation Systems Center, Cambridge, Mass.

was solved by Harris & Reid (1964) using a direct numerical method. The same method was used by Sparrow, Munro & Jonsson (1964) to treat problems over a wide range of radius ratios η ($= R_1/R_2$, where R_1 and R_2 are radii of the inner and outer cylinders respectively). Walowit, Tsao & DiPrima (1964) treated the wide-gap problem using the Galerkin method. When the gap is large and at the same time $\mu < -0{\cdot}5$, the Galerkin method becomes tedious algebraically because a large number of terms need to be used. With the direct numerical method, the set of simultaneous linear algebraic equations which must be solved to obtain the critical conditions becomes linearly dependent and no solution can be found.

In this paper, we discard at the outset the assumption that the time dependence of perturbation quantities is of exponential form. Small random disturbances which are periodic in the axial direction are distributed initially throughout the fluid. Their development in time is obtained by numerical integration. The flow is classified as stable or unstable on the basis of the decay or growth of the kinetic energy of the perturbations. The neutral state is defined by the condition that the perturbation kinetic energy neither grows nor decays in the mean.

With this method, the initial perturbation could vary in the azimuthal direction. However, in the present analysis, axisymmetric disturbances are assumed. The observations in I indicated that, for most of the time, the vortex pattern was not axisymmetric. It is difficult to discern, however, whether the asymmetry was the result of nonlinear interaction of finite amplitude disturbances which had evolved from initially symmetric perturbations, or was the result of the growth of the initially non-axisymmetric linear perturbations to finite amplitude. The results obtained for homogeneous fluids by Krueger, Gross & DiPrima (1966) indicated that for $\mu \sim -1$ non-axisymmetric disturbances may cause a 10% decrease in both the critical Reynolds number and wavenumber. Snyder (1968) found, however, that at $\eta = 0{\cdot}5$ the difference in the critical Reynolds number caused by non-axisymmetric disturbances is only slightly larger than the experimental scatter. In view of these facts, axisymmetric perturbations should yield reasonable results.

The mathematical formulation of the stability problem is described in §2; difference equations are also presented, and the computation procedure discussed. The results are presented in §3. The stabilizing influence of an increase in density gradient is confirmed. Preferred theoretical wavelengths are not in complete agreement with experimental results; however, the critical conditions predicted are reasonable. From streamline plots, we find that the assumption of axisymmetric disturbances results in less complicated cell patterns than are observed.

2. Stability analysis

2.1. *Governing equations*

A cylindrical co-ordinate system (r', θ, z') is chosen such that the z' axis is along the axis of the two concentric cylinders of radii R_1 and R_2 ($R_1 < R_2$). The perturbation velocity components in the r', θ and z' directions are u', v' and w', with pressure and salinity denoted by p' and S'. The system of equations describing the flow consists of the equations of motion with the Boussinesq approximation, the salt

diffusion equation and the continuity equation. The equation of state for the stratified salt solution is taken as

$$\rho' = \rho_0'[1+\beta(S'-S_0')],$$

where β is the coefficient of volume expansion. By assuming axisymmetric perturbations periodic in z' with wavelength $2\pi/\alpha$ in the velocity components, pressure and salinity, the linearized disturbance equations become, after eliminating w' and p',

$$2\frac{V'v'}{\nu r'}\alpha^2 - g\alpha\frac{\beta}{\nu}D'S' = \left[D'D_*' - \alpha^2 - \frac{1}{\nu}\frac{\partial}{\partial t}\right](D'D_*' - \alpha^2)\,u', \tag{1}$$

$$u'\frac{D_*'V'}{\nu} = \left[D'D_*' - \alpha^2 - \frac{1}{\nu}\frac{\partial}{\partial t}\right]v', \tag{2}$$

$$-\left(\frac{dS'}{dz'}\right)_0\frac{D'D_*'u'}{\alpha\kappa_s} = \left[D'D_*' - \alpha^2 - \frac{1}{\kappa_s}\frac{\partial}{\partial t}\right]D'S', \tag{3}$$

where $D' = \partial/\partial r'$ and $D_*' = D' + 1/r'$. In the above equations ν is the kinematic viscosity, κ_s is the coefficient of diffusion for salt and V' is the basic flow velocity. A subscript zero denotes a quantity evaluated in some reference state, usually at the midheight of the stratified fluid. The initial stabilizing density gradient is incorporated into the system as $(dS'/dz')_0$.

To provide a more convenient system to solve, both sides of (3) have been operated on by D'. After using the continuity equation, the boundary conditions become

$$u' = v' = D'u' = D'S' = 0 \quad \text{at} \quad r = R_1, R_2. \tag{4}$$

All physical variables are rendered dimensionless by normalizing all lengths with respect to R_1 and all velocities with respect to $R_1\Omega_1$. A dimensionless wavenumber is defined as $K = \alpha R_1$ and non-dimensional time as $\tau = \nu t/R_1^2$. It is noted that the product $\beta S'$ is non-dimensional. The Reynolds numbers of the inner and outer cylinders are defined as $Re_1 = R_1^2\Omega_1/\nu$ and $Re_2 = R_2^2\Omega_2/\nu$; the Froude number is defined as

$$Fr = \Omega_1/(g/R_1)^{\frac{1}{2}}. \tag{5}$$

Substituting the dimensionless variables into (1)–(3), the following system of linearized disturbance equations is obtained:

$$\left[DD_* - K^2 - \frac{\partial}{\partial\tau}\right](DD_* - K^2)\,u = Re_1\left[2K^2\frac{V}{r}v - Fr^{-2}KD\beta S\right], \tag{6}$$

$$[DD_* - K^2 - \partial/\partial\tau]\,v = Re_1 uD_*V, \tag{7}$$

$$\left[DD_* - K^2 - \frac{\nu}{\kappa_s}\frac{\partial}{\partial\tau}\right]D\beta S = \frac{Re_1}{K}\frac{\nu}{\kappa_s}\beta\left(\frac{dS}{dz}\right)_0 DD_*u, \tag{8}$$

where the dimensionless variables appear unprimed. The boundary conditions become

$$u = v = D_*u = DS = 0 \quad \text{at} \quad r = 1, \eta^{-1}. \tag{9}$$

The tangential velocity of the basic flow may be computed from the steady solution of the equations of motion, which in non-dimensional form is

$$V = \frac{(\mu - \eta^2) r}{1 - \eta^2} + \frac{1 - \mu}{(1 - \eta^2) r}. \tag{10}$$

Following Chen & Kirchner (1971) equations (6)–(8) are solved using numerical means. By introducing

$$\xi = (DD_* - K^2) u, \tag{11}$$

which is essentially the axial derivative of the linearized azimuthal vorticity, and letting

$$\Theta = DS, \tag{12}$$

(6)–(8) become

$$\frac{\partial \xi}{\partial \tau} = [DD_* - K^2] \xi - Re_1 \left[2K^2 \frac{V}{r} v - Fr^{-2} K \beta \Theta \right], \tag{13}$$

$$\frac{\partial v}{\partial \tau} = [DD_* - K^2] v - Re_1 u D_* V, \tag{14}$$

$$\frac{\partial \Theta}{\partial \tau} = \frac{\kappa_s}{\nu} [DD_* - K^2] \Theta + \frac{Re_1}{K} \left(\frac{dS}{dz} \right)_0 DD_* u, \tag{15}$$

with the boundary conditions

$$u = v = D_* u = \Theta = 0 \quad \text{at} \quad r = 1, \eta^{-1}. \tag{16}$$

Equations (13)–(15) prescribe the development in time of ξ, v and Θ; equation (11) defines ξ in terms of u, and (12) defines Θ in terms of S. The boundary conditions on ξ may be obtained from (11) by making use of the boundary conditions on u given in (16):

$$\xi = \partial^2 u / \partial r^2 \quad \text{at} \quad r = 1, \eta^{-1}. \tag{17}$$

The stream function ψ may be obtained from the definition

$$u' = r'^{-1} \partial \psi' / \partial z'. \tag{18}$$

After linearization and assumption of an axisymmetric perturbation

$$\psi'(r', t) \sin \alpha z'$$

the disturbance stream function becomes

$$\psi = ur / K. \tag{19}$$

The perturbation kinetic energy E per wavelength normalized with respect to the constant $\pi \rho R_1^5 \Omega_1^2 / K$ is defined as follows:

$$E = \pi \int_1^{\eta^{-1}} r \left[u^2 + v^2 + \frac{1}{K^2} (D^* u)^2 \right] dr. \tag{20}$$

2.2. *Difference equations*

Depending on whether the cylinders are rotating in the same direction or in opposite directions, the annular region $1 \leqslant r \leqslant R_2/R_1$ is either divided into equal grid increments or considered as two subregions separated by the location R_0 where the tangential basic flow velocity is zero, the two subregions $1 \leqslant r \leqslant R_0$

and $R_0 \leqslant r \leqslant R_2/R_1$ each being divided into equal grid increments. Physically, there is a certain cylindrical surface, at R_0, between two counter-rotating cylinders which divides the flow. In the inner subregion $1 \leqslant r \leqslant R_0$ the flow is characteristically unstable in that the square of the circulation decreases outwards; calculations performed across the inner subregion strongly influence the solution of the stability problem. Should the grid increments for cylinders rotating in the same direction be retained for counter-rotating cylinders, there would be only a few grid points in the most critical region. With increasingly negative speed ratios, the inner subregion $1 \leqslant r \leqslant R_0$ becomes smaller. By considering the annular region as two subregions, it is possible to assign grid increments to each subregion which give results with counter-rotating cylinders of comparable accuracy to results with corotating cylinders.

The ξ equation (11), when written in finite-difference form, results in a tridiagonal matrix, which may be solved by Gaussian elimination (see for example Keller 1968, p. 76). The boundary conditions on ξ are obtained using $Du = 0$ in (17), and the fact that u would be symmetric about the boundary

$$\xi_1^n = 2u_1^n/(\Delta r)^2, \quad \xi_{JN} = 2u_{JN-1}/(\Delta r)^2, \tag{21}$$

where the subscripts $j = 1$ and $j = JN$ indicate grid points at the boundaries $r = 1$ and $r = R_2/R_1$.

The parabolic equations (13)–(15) are solved using an explicit finite-difference scheme of integration. This scheme has the advantage of requiring knowledge of variables at only one previous time step, and does not require an iterative procedure. The solution algorithms for ξ, v and H reduce to a fairly compact form with coefficients with common subscripts which minimize computer storage. The equations are presented in terms of a general variable Q. The time-advanced $(n+1)$th value of Q at the jth grid point is

$$Q_j^{n+1} = \frac{\Delta\tau}{(\Delta r)^2}\left\{\frac{1}{\Lambda}\left[\alpha_j Q_{j+1}^n + \sigma_j Q_{j-1}^n - \left(\frac{(\Delta r)^2}{\Delta\tau}\Lambda - \omega_j\right) Q_j^n\right] + F_j(Q)\right\}, \tag{22}$$

where

$$F_j(Q) = \begin{cases} -2Re_1 K\,(V_j^n/r_j)\,v_j^n(\Delta r)^2 + Re_1 Fr^{-2} K\beta\Theta_j^n(\Delta r)^2, & Q = \xi, \quad \Lambda = 1, \\ -\tfrac{1}{2}Re_1(\Delta r)\,u_j^n\,[V_{j+1}^n - V_{j-1}^n + 2(\Delta r)\,V_j^n/r_j], & Q = v, \quad \Lambda = 1, \\ \dfrac{Re_1}{K}\left(\dfrac{dS}{dz}\right)_0 [\alpha_j u_{j+1}^n + \sigma_j u_{j-1}^n + \epsilon_j u_j^n], & Q = \Theta, \quad \Lambda = \dfrac{\nu}{\kappa_s}, \end{cases}$$

with

$$\alpha_j = 1 + \Delta r/2r_j, \quad \sigma_j = 1 - \Delta r/2r_j,$$

$$\omega_j = 2 + (\Delta r)^2\,[K^2 - 1/r_j^2], \quad \epsilon_j = 1 + (\Delta r/r_j)^2.$$

The value of $\Delta\tau$ is chosen such that $\Delta\tau/(\Delta r)^2 \leqslant 0{\cdot}5$ to ensure numerical stability.

The boundary conditions for the perturbation velocities and salinity are, using the same subscript notation as in (22),

$$\left.\begin{aligned} u_1 = v_1 = D_* u_1 = \Theta_1 \\ u_{JN} = v_{JN} = D_* u_{JN} = \Theta_{JN} \end{aligned}\right\} = 0 \quad \text{for all } n. \tag{23}$$

2.3. *Calculation procedure*

The calculation procedure is initiated by setting all variables equal to zero, followed by assigning small random values of ξ at the interior grid points $1 < r < JN$. Random values of ξ are generated by the subroutine RANDU of the IBM system/360 scientific subroutine package with values between 0 and 1; these numbers are multiplied by 10^{-4} to ensure that the initial disturbances are small. The boundary values of ξ are not known *a priori*, since they depend on the second derivative of u. By solving (11) for u, the boundary values of ξ are obtained from (17). The time-advanced ξ, u and Θ values are then computed using (13)–(15). The perturbation kinetic energy is calculated according to (20) using Simpson's rule, and the stream function is computed from (19). This calculation procedure is repeated for subsequent time steps using the computed boundary values of ξ.

The perturbation kinetic energy E is normalized with respect to its initial value computed at $\tau = 0$, and is used to monitor the behaviour of the disturbances. The growth or decay of E determines whether the flow is unstable or stable. The oscillatory nature of E will be discussed in the following section, but pertinent here is the fact that this oscillatory behaviour limits the number of time steps which may be computed between printouts for meaningful interpretation of the results. Printing results at each time step avoids this situation, but results in voluminous output. In order to follow the trend of the oscillations, results are usually printed at intervals corresponding to approximately 10 % of the oscillation period. The oscillation periods and number of calculation time steps per period vary with the speed ratio, wavenumber and Reynolds number; hence, printout times must be adjusted for each case.

3. Results and discussion

The results of stability calculations are presented for cylinders having a radius ratio η of 0·2 and for stable density gradients ϕ_0 of $-0{\cdot}0011$ and $-0{\cdot}0021$. These density gradients approximate conditions used in the physical experiments reported in I, and are defined as

$$\phi_0 = \beta(dS/dz)_0. \tag{24}$$

The corresponding buoyancy frequencies are 0·904 and 1·267 s^{-1}. In the calculations the ratio ν/κ_s was set to be 700. Calculated results are presented in table 1. Sixteen cases are listed, each representing only the final results of a series of trials to determine the critical conditions for a given density gradient and speed ratio. Generally, 10 trials were necessary to obtain the critical Reynolds number Re_1 of the inner cylinder. The first three cases are for the smaller density gradient of $-0{\cdot}0011$, with the remaining cases for the larger gradient of $-0{\cdot}0021$. For comparison of predicted stability conditions with the physical experiments previously referred to, a range of speed ratios from $-1{\cdot}00$ to 0·02 was considered at $\phi_0 = -0{\cdot}0021$. Perturbations were introduced into the tangential basic flow

Case	Speed ratio, μ	Wavenumber, K	Reynolds number of inner cylinder, Re_1	Froud number Fr
		$\phi_0 = -0{\cdot}0011$, $\nu = 0{\cdot}00988\,\mathrm{cm^2\,s^{-1}}$		
1	0	12·85†	196·2	0·0213
2	0	16·00	186·7	0·0203
3	0	18·00	196·2	0·0213
		$\phi_0 = -0{\cdot}0021$, $\nu = 0{\cdot}01033\,\mathrm{cm^2\,s^{-1}}$		
4	0·02	14·00†	314·6	0·0358
5	0·02	16·00	295·7	0·0337
6	0·02	18·00	294·0	0·0335
7	0·0	14·00	236·9	0·0270
8	0·9	16·00†	222·5	0·0254
9	0	18·00	221·5	0·0253
10	0	20·00	231·5	0·0264
11	−0·02	16·00	195·0	0·0222
12	−0·02	18·00	193·4	0·0220
13	−0·02	20·00	201·0	0·0229
14	−0·10	16·81†	181·3	0·0206
15	−0·50	24·55†	163·8	0·0186
16	−1·00	28·35†	231·5	0·0263

† Experimentally determined preferred wavenumber.

TABLE 1. Calculated results, $\eta = 0{\cdot}2$

at $\tau = 0$, and stability conditions determined by monitoring the development of the perturbation kinetic energy E in time. During these calculations the gap width $d\,(= R_1 - R_2)$ was used as the basic length parameter. However, the results were converted and are presented with R_1 as the basic length.

This method of analysis was first used to solve the homogeneous Couette flow stability problem with a wide gap and negative speed ratios. From these results guidelines were obtained as to the number J of grid increments required across the gap, and an estimate was made of the accuracy of the calculations. The results of the analysis for the homogeneous case at $Re_1 = 114{\cdot}0$, $K = 3{\cdot}06$, $\mu = -0{\cdot}5$ and $\eta = 0{\cdot}5$ are shown in figure 1. The two curves for $J = 40$ and 80 show the variation of the perturbation kinetic energy E with non-dimensional time τ, where J is the number of equal-sized grid increments across the gap and E is normalized with respect to its value at $\tau = 0$. The critical Re_1 is taken to be that at which E neither grows nor decays as $\tau \to \infty$. Both curves initially show a decrease in E, followed by a sharp rise and a subsequent decline. At approximately $\tau = 0{\cdot}065$ both curves begin to rise, but the curve for $J = 80$ levels off at $E = 1$ for $\tau > 0{\cdot}09$. The levelling off of the curve indicates that the critical conditions are satisfied for the case $J = 80$, while the increasing E curve at $J = 40$ indicates that $Re_1 = 114{\cdot}0$ is supercritical. Sparrow *et al.* (1964) determined the critical Reynolds number at the same value of K as 114·75, which is approximately a 0·7 % difference from the present calculation. On the basis of these considerations, preliminary calculations were made for the stratified case using $J = 40$ and 80.

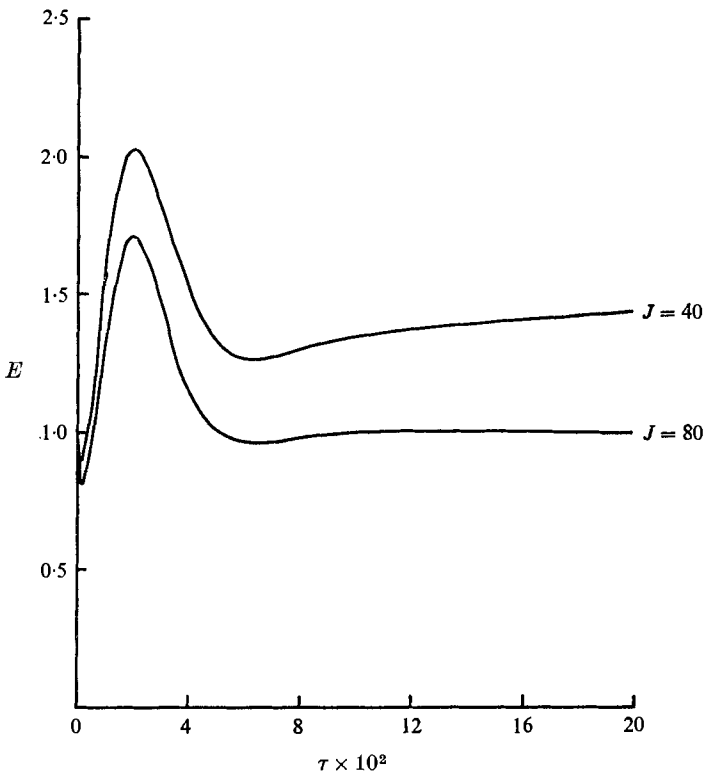

FIGURE 1. Effect of $J = 40$ and 80 grid increments on the perturbation kinetic energy for homogeneous fluid at $Re_1 = 114{\cdot}0$, $K = 3{\cdot}06$, $\mu = -0{\cdot}5$ and $\eta = 0{\cdot}5$.

Preliminary calculations made for the stratified case showed that the E curve was of an oscillatory nature and did not become monotonic after a finite time τ as did the previously described homogeneous E curve. Initial attempts to break down the annular gap into equal increments with $J = 40$ and 80 indicated that for counter-rotating cylinders there was not a sufficient number of grid points in the most critical region of the gap, $R_1 \leqslant r \leqslant R_0$. Such calculations showed general agreement with experimental results of I for $\mu \geqslant 0$, but predicted unreasonably high values of the critical Reynolds number for $\mu < 0$. Using the divided grid scheme previously described for counter-rotating cylinders, the number of grid points was increased in the region $R_1 \leqslant r \leqslant R_0$ and trial calculations were made with $J = 40$, 80 and 160. The remainder of the gap, $R_0 \leqslant r \leqslant R_2$, was assigned $J = 40$. Figure 2 shows the results of calculations made at

$$Re_1 = 171{\cdot}5, \quad K = 16{\cdot}0, \quad \mu = -0{\cdot}1, \quad \eta = 0{\cdot}2 \quad \text{and} \quad \phi_0 = -0{\cdot}0021.$$

For $J = 40$ the perturbation kinetic energy curve is seen to oscillate with an increasing trend, while the curves for $J = 80$ and 160 show decreasing trends or stable conditions with relatively good agreement in the amplitudes up to $\tau = 0{\cdot}015$. It is noted that in subsequent determinations of critical conditions it was usually sufficient to carry out the integration to $\tau \sim 0{\cdot}02$.

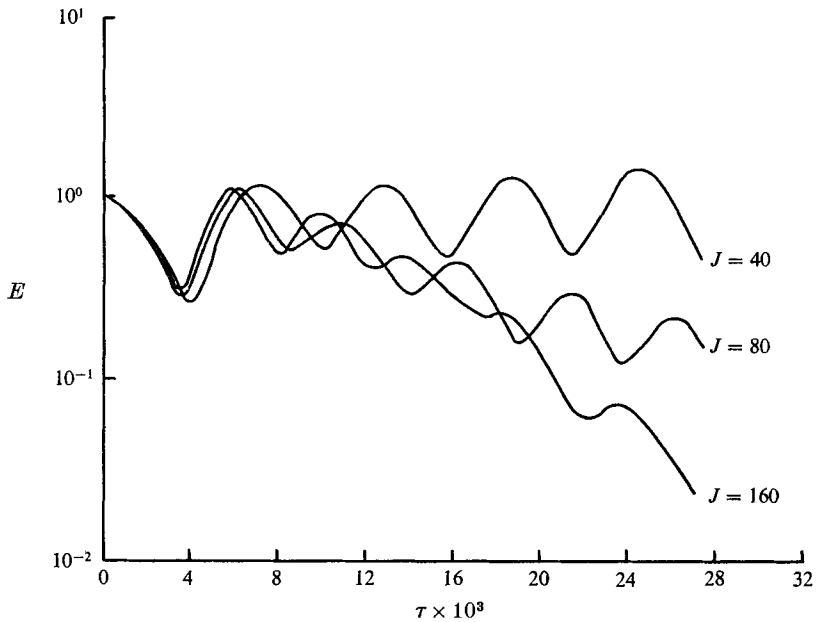

FIGURE 2. Effect of $J = 40$, 80 and 160 grid increments on the perturbation kinetic energy at $Re_1 = 171{\cdot}5$, $K = 16{\cdot}00$, $\mu = -0{\cdot}1$, $\eta = 0{\cdot}2$ and $\phi_0 = -0{\cdot}0021$.

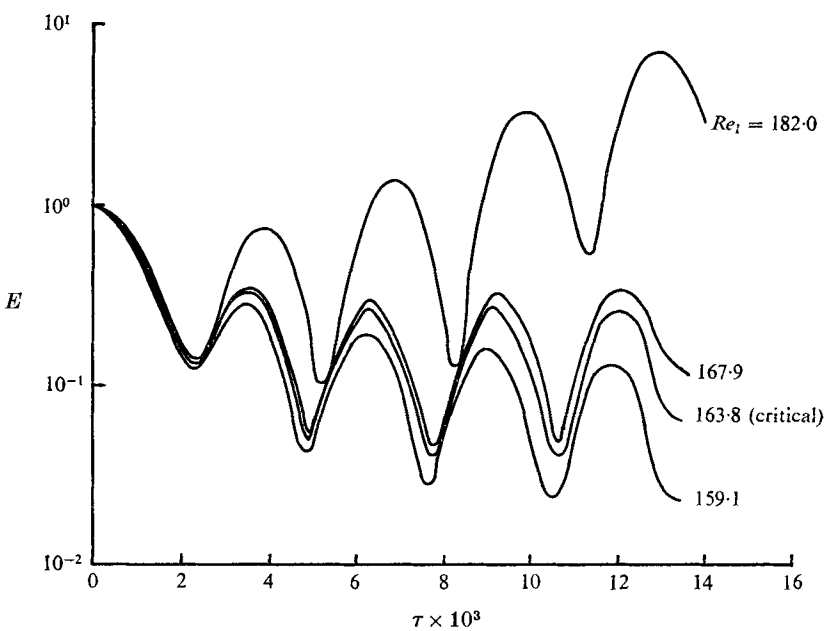

FIGURE 3. Determination of critical Reynolds number for $K = 24{\cdot}55$, $\mu = -0{\cdot}5$, $\eta = 0{\cdot}2$ and $\phi_0 = -0{\cdot}0021$.

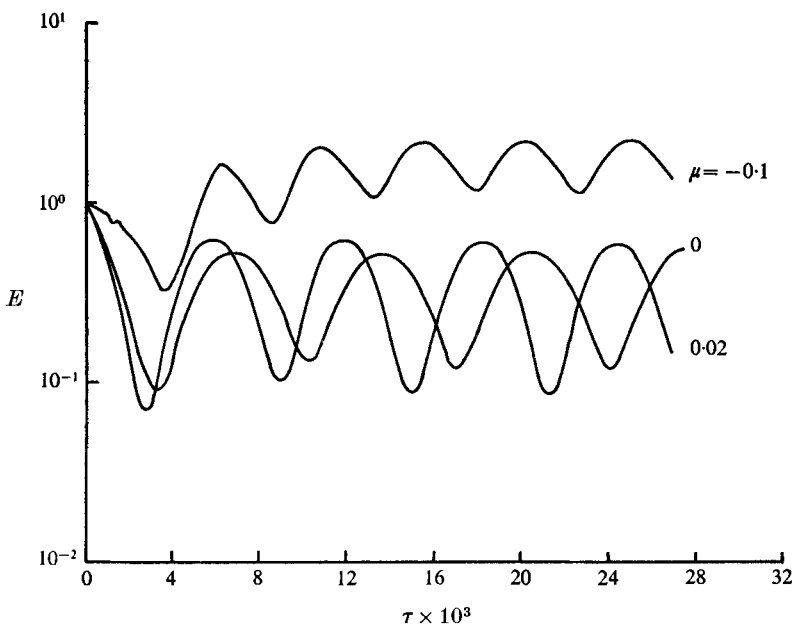

FIGURE 4. Perturbation kinetic energy at critical Reynolds numbers for $\mu = -0{\cdot}1$, $Re_1 = 181{\cdot}3$, $K = 16{\cdot}81$; $\mu = 0$, $Re_1 = 222{\cdot}5$, $K = 16{\cdot}00$; and $\mu = 0{\cdot}02$, $Re_1 = 314{\cdot}6$, $K = 14{\cdot}00$. Calculations made at $\eta = 0{\cdot}2$ and $\phi_0 = -0{\cdot}0021$.

On the basis of the experience gained from trial calculations made for both the homogeneous and stratified cases, for positive speed ratios the entire gap $R_1 \leqslant r \leqslant R_2$ was divided into $J = 160$ equal grid increments, and for $\mu < 0$ the gap region $R_1 \leqslant r \leqslant R_0$ was divided into 160 increments. Thus it is expected that the accuracy for the computations made in the regions where instability is most likely to occur is approximately the same for all speed ratios.

Figure 3 illustrates the procedure for determining the critical Reynolds number at $K = 24{\cdot}55$, $\mu = -0{\cdot}5$, $\eta = 0{\cdot}2$ and $\phi_0 = -0{\cdot}0021$. The experimental results of I are used as a guide for selecting trial values of the critical Reynolds number. By performing calculations over a range of values of Re_1, the critical value is bracketed as shown by the four curves. $Re_1 = 182{\cdot}0$ exceeds the critical value as is indicated by the increasing trend of the maximum points on the oscillating E curve. The lowest curve, for $Re_1 = 159{\cdot}1$, is below that for the critical Reynolds number by only approximately 3 %, but exhibits a relatively strong decreasing trend. The trend of the kinetic energy is established after the second maximum point of the curve; at the critical value of Re_1 the maximum points may oscillate by approximately $\pm 0{\cdot}5$ %. Therefore, it is always necessary to compute at least three maximum points to establish a trend. The criterion for selection of the critical Re_1 is to take the Re_1 corresponding to the curve for which the maximum values of the perturbation kinetic energy neither grow nor decay as τ increases.

Perturbation kinetic energy curves at critical conditions for $\mu = 0{\cdot}02$, 0 and $-0{\cdot}1$ with $\phi_0 = -0{\cdot}0021$ are shown in figure 4. These three cases compare the typical behaviour of the E curves for positive, zero and negative speed ratios.

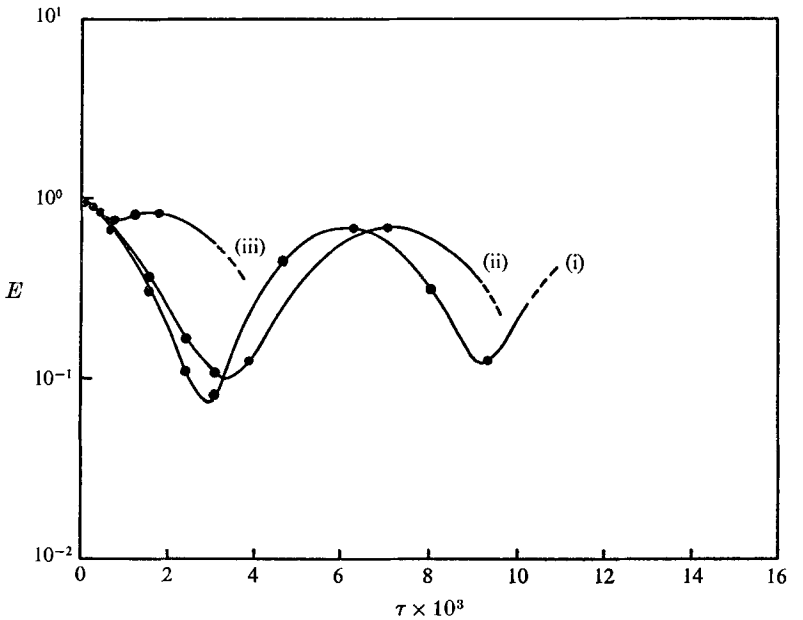

FIGURE 5. Perturbation kinetic energy corresponding to cases shown in streamline plots. (i) $Re_1 = 326{\cdot}0$, $K = 14{\cdot}00$, $\mu = 0{\cdot}02$. (ii) $Re_1 = 235{\cdot}0$, $K = 15{\cdot}70$, $\mu = 0$. (iii) $Re_1 = 193{\cdot}2$, $K = 16{\cdot}81$, $\mu = -0{\cdot}1$. Calculations made at $\eta = 0{\cdot}2$ and $\phi_0 = -0{\cdot}0021$.

The highest level of perturbation kinetic energy is attained for $\mu = -0{\cdot}1$. The level of E for the case $\mu = 0{\cdot}02$ is lower than that for $\mu = -0{\cdot}1$, but is above the level of E attained in the case $\mu = 0$. In the cases where the outer cylinder is rotating there is more energy available in the basic flow to feed the perturbations, and this is revealed by the correspondingly higher E levels. The oscillation period $\Delta\tau_p$ of the perturbation kinetic energy is seen to vary with μ. The lowest oscillation period for the cases under consideration is $\Delta\tau_p = 0{\cdot}005$ for $\mu = -0{\cdot}1$; the period is greater for $\mu = 0$, being $\Delta\tau_p = 0{\cdot}007$, and is reduced to $\Delta\tau_p = 0{\cdot}006$ at $\mu = 0{\cdot}02$. The corresponding frequencies are 7·25, 5·17, and 6·04 s^{-1}, which are about five times the buoyancy frequency. These oscillations are the result of periodic splitting and recombining of the azimuthal vortices as revealed by streamline plotting discussed below.

The calculated flow field is described by streamline plots at selected times, which are indicated as dots along the perturbation kinetic energy curves in figure 5. Three cases are shown in the streamline plots of figures 6, 7 and 8, which represent the cases of positive, zero and negative speed ratios respectively. The Reynolds number Re_1 is approximately 10 % above the critical value for each of the three speed ratios, $\mu = 0{\cdot}02$, 0 and $-0{\cdot}1$. The plots were obtained from the same plotter routine as was used by Liu & Chen (1973).

Figure 5 is a plot of the initial segments of the perturbation kinetic energy curves for the cases presented in the streamline plots. The dots on each curve correspond to the times for which streamline plots are shown. In each streamline plot the left and right vertical boundaries represent the surfaces of the inner and

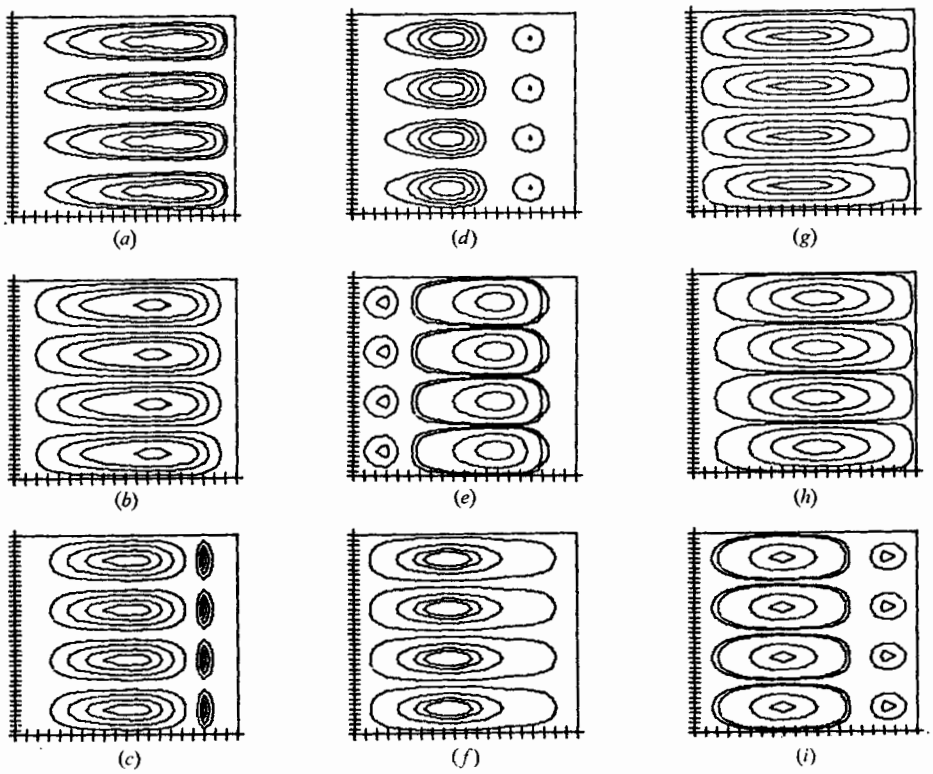

FIGURE 6. Streamline plots with cylinders rotating in the same direction at $Re_1 = 326{\cdot}0$, $K = 14{\cdot}00$, $\mu = 0{\cdot}02$, $\eta = 0{\cdot}2$ and $\phi_0 = -0{\cdot}0021$. Dimensionless times: (*a*) $0{\cdot}781 \times 10^{-4}$, (*b*) $0{\cdot}765 \times 10^{-3}$, (*c*) $0{\cdot}154 \times 10^{-2}$, (*d*) $0{\cdot}232 \times 10^{-2}$, (*e*) $0{\cdot}310 \times 10^{-2}$, (*f*) $0{\cdot}467 \times 10^{-2}$, (*g*) $0{\cdot}623 \times 10^{-2}$, (*h*) $0{\cdot}779 \times 10^{-2}$, (*i*) $0{\cdot}935 \times 10^{-2}$.

outer cylinders, respectively. The horizontal lines at the top and bottom are fictitious periodic boundaries at an axial distance of two wavelengths. The use of two wavelengths was selected by Liu & Chen (1973) to generate symmetrical cells during a numerical wavenumber search, and is retained here primarily for convenience. The grid marks shown divide each wavelength and the annular gap width into 20 increments. Plots for $\mu < 0$ show a vertical line through the location R_0 where the basic flow velocity vanishes.

Figure 6 illustrates the development of the perturbation streamlines at selected time intervals for the case $Re_1 = 326$, $K = 14{\cdot}00$, $\mu = 0{\cdot}02$, $\eta = 0{\cdot}2$ and $\phi_0 = -0{\cdot}0021$. The first plot (figure 6 *a*) shows the perturbation streamlines after five calculation cycles from $\tau = 0$. It shows that the initial random disturbances are quickly organized into vortex motion. The development of a secondary vortex system near the wall of the outer cylinder is shown in the next three plots. The secondary cells appear to be growing at the expense of the larger inner cells. In figure 6(*e*), the smaller vortex system becomes the larger, which occurs in this case just after E has its first minimum point. The initially larger cells are no longer present in figure 6(*f*). The next picture (figure 6*g*) shows the initially smaller vortices growing to approximately their largest size, which occurs im-

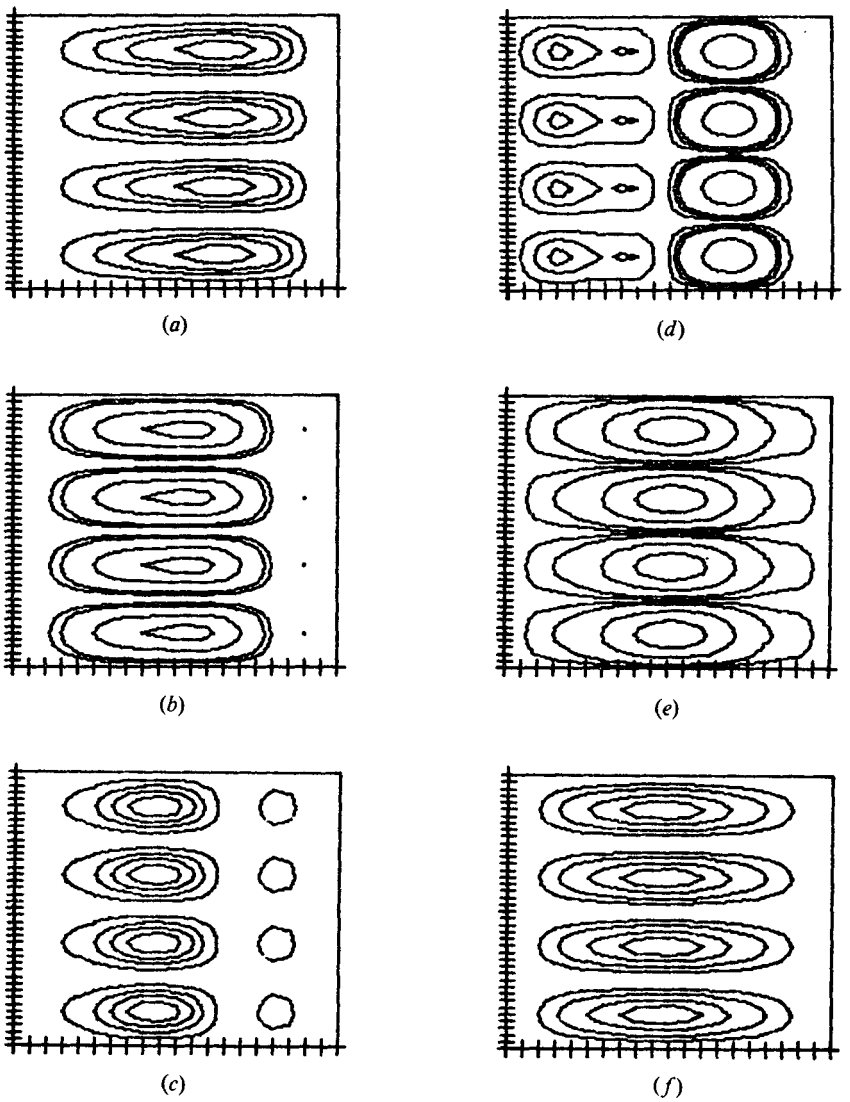

FIGURE 7. Streamline plots with rotating inner cylinder and stationary outer cylinder at $Re_1 = 235{\cdot}0$, $K = 15{\cdot}70$, $\mu = 0$, $\eta = 0{\cdot}2$ and $\phi_0 = -0{\cdot}0021$. Dimensionless times: (*a*) $0{\cdot}765 \times 10^{-3}$, (*b*) $0{\cdot}154 \times 10^{-2}$, (*c*) $0{\cdot}232 \times 10^{-2}$, (*d*) $0{\cdot}310 \times 10^{-2}$, (*e*) $0{\cdot}389 \times 10^{-2}$, (*f*) $0{\cdot}701 \times 10^{-2}$.

mediately after E passes through its first maximum point at the completion of its first oscillation. The last two pictures (figures 6*h*, *i*) show that a secondary vortex develops again near the wall of the outer cylinder in a similar manner to the system previously developed during the first half of the initial cycle. The final plot (figure 6*i*) corresponds to a time just after E passes through its second minimum point. For this particular set of streamline plots there is a general correlation between the minimum energy point and the two-vortex system, and between the maximum energy point and the fully developed one-vortex system. This correlation holds for $\mu \geqslant 0$ cases but not for $\mu < 0$ cases.

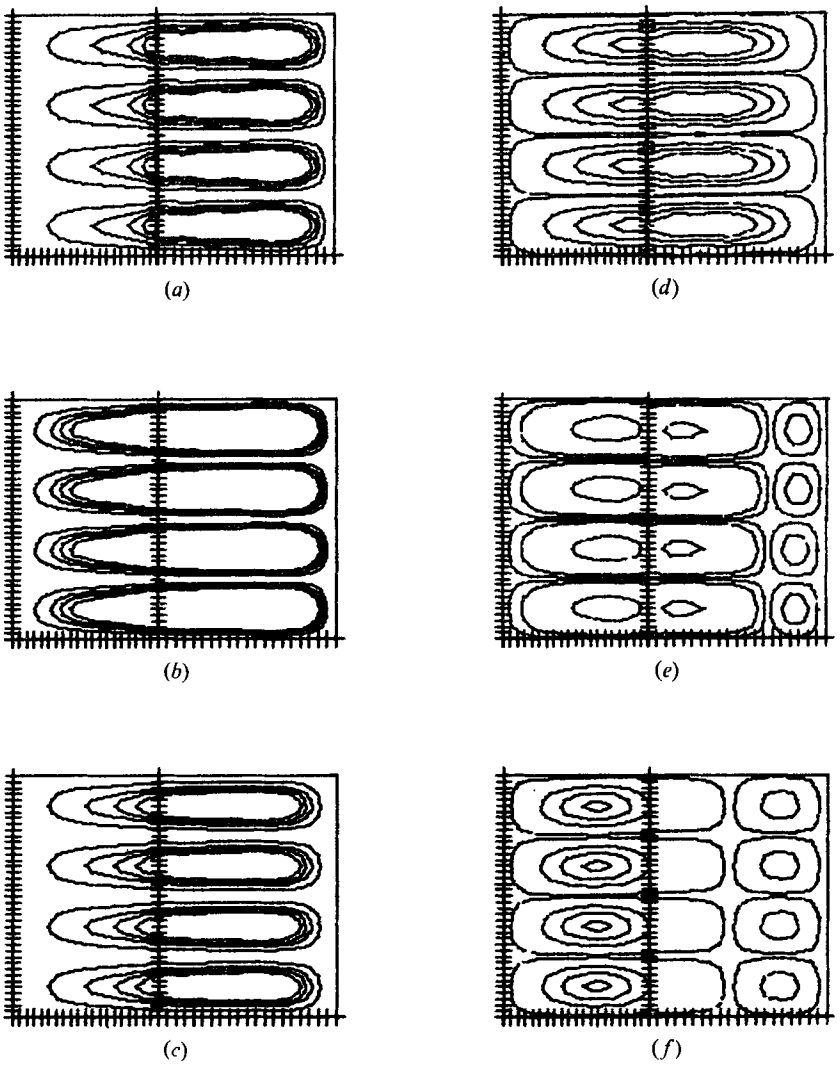

FIGURE 8. Streamline plots with counter-rotating cylinders at $Re_1 = 193{\cdot}2$, $K = 16{\cdot}81$, $\mu = -0{\cdot}1$, $\eta = 0{\cdot}2$ and $\phi_0 = -0{\cdot}0021$. Dimensionless times: (*a*) $0{\cdot}149 \times 10^{-3}$, (*b*) $0{\cdot}307 \times 10^{-3}$, (*c*) $0{\cdot}466 \times 10^{-3}$, (*d*) $0{\cdot}784 \times 10^{-3}$, (*e*) $0{\cdot}126 \times 10^{-2}$, (*f*) $0{\cdot}173 \times 10^{-2}$.

Streamline plots for $\mu = 0$ are shown in figure 7 for $Re_1 = 235$, $K = 15{\cdot}70$, $\eta = 0{\cdot}2$ and $\phi_0 = -0{\cdot}0021$. The wavelength of the disturbances for this case is approximately 5 % smaller than for the case at $\mu = 0{\cdot}02$ as indicated by the reduction in height of the vertical walls. In figure 7(*a*) the streamlines are depicted after 50 calculation cycles and are seen to be similar to the previous case. The origin of a secondary vortex system near the outer wall is seen in figure 7(*b*). The secondary cells grow to approximately the size of the initially larger cells in figure 7(*d*), and finally engulf the initial cells in figure 7(*e*). The times corresponding to figures 7(*d*) and (*e*) bracket the minimum energy point. In figure 7(*f*) the streamlines are for a time near the first maximum of the energy

curve. For this set of streamline plots, the general conditions found for case $\mu = 0{\cdot}02$ hold.

The development of the perturbation stream function for $Re_1 = 193{\cdot}2$, $K = 16{\cdot}81, \mu = -0{\cdot}1, \eta = 0{\cdot}2$ and $\phi_0 = -0{\cdot}0021$ is shown in figure 8. A reduction in wavelength of 15% from that in the case $\mu = 0{\cdot}02$ is shown by the smaller vertical walls. The vertical line near the centre of each picture indicates the location of R_0, which is at $0{\cdot}45d$ for $\mu = -0{\cdot}1$. Shown in the first picture (figure 8*a*) are the streamlines after 50 calculation cycles. The non-dimensional time reached after 50 calculation cycles for $\mu = -0{\cdot}1$ is approximately one fifth of the time reached after the same number of cycles at $\mu = 0$ owing to the smaller grid spacing. These cells become progressively weaker and in figure 8(*d*) the value of E has reached its minimum. The subsequent formation of a secondary system near the outer wall is shown in figure 8(*e*). It is interesting to note that there are three vortex systems in figure 8(*e*), which develop into the two-vortex system as shown in figure 8(*f*). The energy curve is at its first maximum value at this time.

It appears that for $\mu \geqslant 0$ the maximum perturbation kinetic energy occurs when the perturbation flow field consists of one large vortex. For counter-rotating flow ($\mu < 0$), however, the maximum perturbation kinetic energy occurs when there are two opposing vortices. This difference may be attributed to the difference in the flow fields of these two cases. When $\mu \geqslant 0$, the tangential velocity within the annulus is of one sign. It is reasonable to expect that a large vortex spanning the entire gap would be more vigorous than two opposing vortices. When $\mu < 0$, the tangential velocity changes sign somewhere within the annulus. Now it is reasonable to expect that two counter-rotating vortices would be more vigorous than one large vortex. It is also interesting to note that, in the streamline plots for $\mu < 0$, the vortex system near the inner wall extends beyond R_0, which is in agreement with the experimental observations of I.

The theoretical cell patterns shown in the streamline plots are based on the assumptions that the disturbances are axisymmetric and periodic in z. As a result, symmetrical Taylor-type cells are generated within an axial distance of one wavelength; they develop into a two-vortex system, and after a time interval, return to the simple Taylor cells. The experimentally determined wave form described in I shows two small cells developing adjacent to the inner cylinder between two larger cells. These smaller cells develop into larger cells until the smaller become the larger and vice versa, and with increasing time the roles of the cells are reversed and the cell pattern returns to its initial configuration. The theoretical development of axisymmetric cells shows a qualitative agreement with the experimental observations in that there is a periodic transformation from development of the one-vortex to the two-vortex system although the periods of the calculated and experimental wave forms are quite different. The effect of non-axisymmetric disturbances on stability has been investigated for the homogeneous case theoretically by Krueger *et al.* (1966) and experimentally by Snyder (1968). Both papers reported that the variation in critical conditions for non-axisymmetric disturbances relative to those for axisymmetric disturbances is small. Snyder (1968), for example, indicated that for $\eta = 0{\cdot}5$ the differences in the

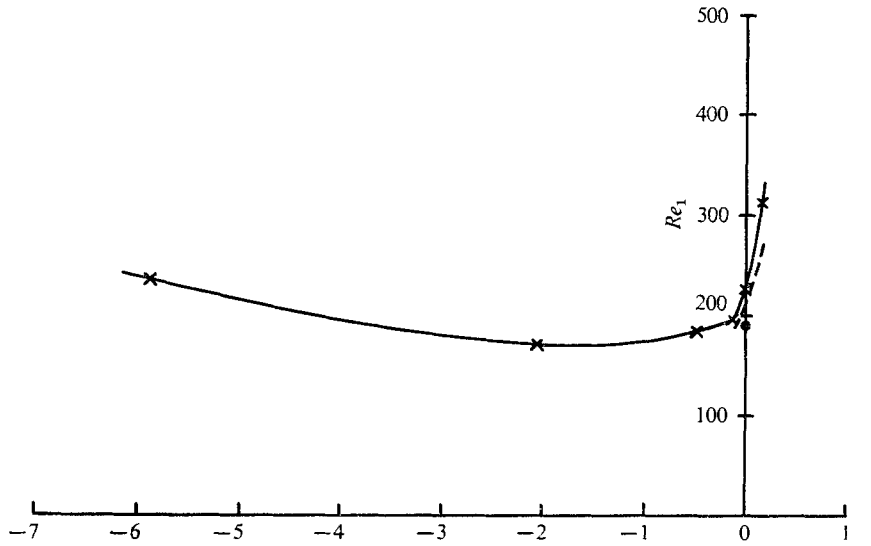

FIGURE 9. Theoretical stability curves at $\eta = 0{\cdot}2$. —×—, calculation with experimental wavelengths from I at $\phi_0 = -0{\cdot}0021$; – – –, calculation with theoretical wavelengths at $\phi_0 = -0{\cdot}0021$; ●, critical condition at $\phi_0 = -0{\cdot}0011$ calculated with experimental wavelength.

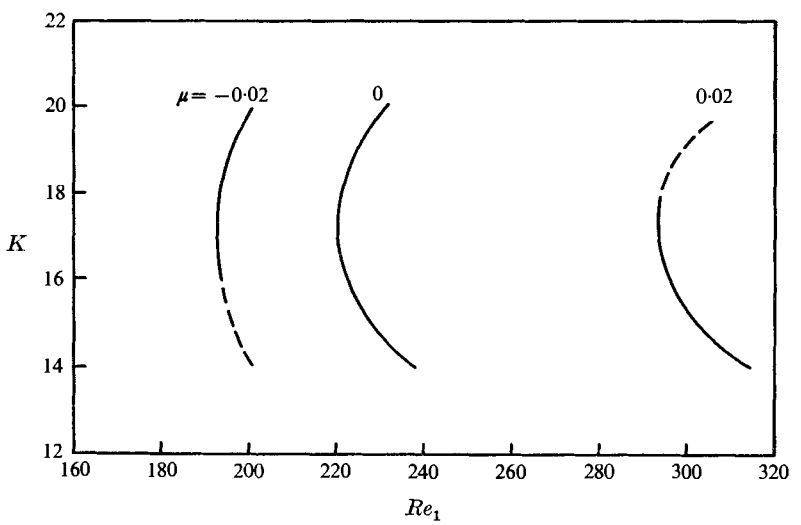

FIGURE 10. Theoretical wavenumber selection for $\mu = -0{\cdot}02$, 0 and 0·02 for $\eta = 0{\cdot}2$ and $\phi_0 = -0{\cdot}0021$.

solutions are only slightly larger than the scatter in experimental data. It is suggested that a similar mechanism of wave-form influence is present in the stratified case, and the computations made with the assumption of axisymmetric wave forms are sufficiently accurate for comparison with the experimental data reported in I.

A stability curve was determined for the case $\eta = 0{\cdot}2$, $\phi_0 = -0{\cdot}0021$ over a range of speed ratios from $-1{\cdot}0$ to 0·02 using wavelengths from the experimental

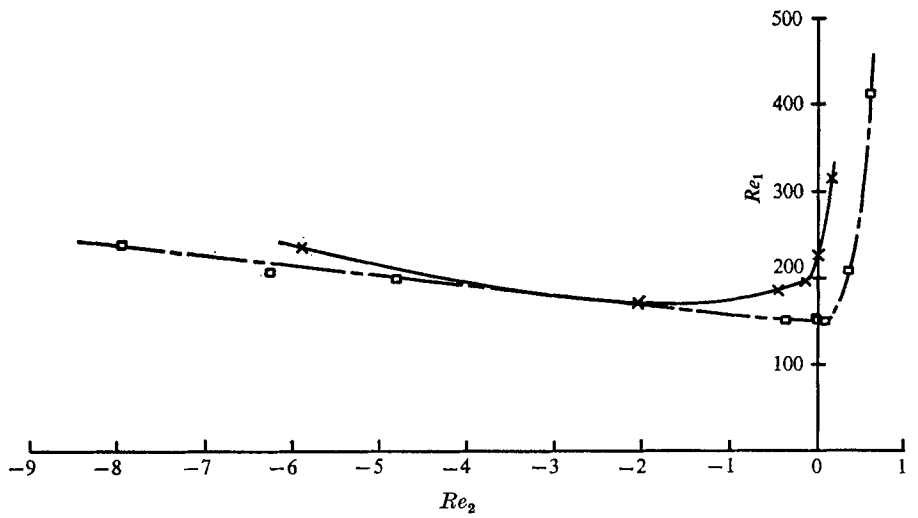

FIGURE 11. Comparison of theoretical and experimental stability curves at $\eta = 0{\cdot}2$. —×—, calculation with experimental wavelengths from I at $\phi_0 = -0{\cdot}0021$; —□—, experimental results from I with $\phi_0 = -0{\cdot}0020$.

data of I. Experimental wavenumbers are indicated with an asterisk in table 1. The stability curve is shown in figure 9, where calculated points are indicated by the crosses on the curve. A minimum point is exhibited by the stability curve at approximately $Re_2 = -2050$. To determine the influence of the density gradient on stability, a case computed with the smaller gradient of $-0{\cdot}0011$ is shown at $Re_2 = 0$. The critical value of Re_1 is approximately 15% less for the smaller density gradient than for the larger density gradient.

The dashed line shows a segment of a stability curve determined with theoretically predicted critical wavenumbers. Theoretical critical wavenumbers and critical Reynolds numbers are obtained from wavenumber *vs.* Reynolds number Re_1 plots as shown in figure 10. Three curves were determined for $\mu = 0{\cdot}02$, 0 and $-0{\cdot}02$ by choosing a range of wavenumbers to bracket the critical value occurring at the minimum value of Re_1. A 7% increase in the critical value of Re_1 was obtained at $\mu = 0{\cdot}02$ when the experimental value $K = 16{\cdot}5$. No systematic search was conducted at all the speed ratios considered for a theoretical critical wavenumber owing to the large computing time required.

In figure 11, the theoretically calculated stability curve is compared with the experimental data from I. In general, the agreement is quite good for negative speed ratios. For speed ratios near and greater than zero, the theoretical curve gives critical values of Re_1 much higher than the experimental values. It is to be noted that the experimental values of the critical Reynolds number for $\mu > 0$ could have been influenced by end effects.

4. Conclusions

In this paper we have presented an analysis of the stability of rotational Couette flow of a stably stratified fluid. A system of time-dependent linearized partial differential equations is solved using explicit finite-difference approximations. Small random perturbations are initially introduced into the flow field, and the state of the flow is examined after finite increments in time. The growth or decay in the mean of the perturbation kinetic energy is used to determine whether the flow is unstable or stable.

Results indicate that the method is applicable to Couette flow stability problems for both homogeneous and stratified fluids. The case of a large gap between counter-rotating cylinders with a large negative speed ratio does not present computational difficulties. Calculations for the homogeneous case are within better than 1 % agreement with the results of Sparrow *et al.* (1964) at a radius ratio of 0·5 and negative speed ratios as large as $-0{\cdot}5$. The method is used to examine the stability of stably stratified Couette flows with a radius ratio of 0·2 and negative speed ratios as large as $-1{\cdot}0$. The theoretical neutral-stability curve best agrees with the experimental results of I for negative speed ratios greater than approximately $-0{\cdot}5$. Calculations confirm the stabilizing influence of an increase in density gradient. Theoretically determined critical wavenumbers do not agree in all cases with the experimentally determined values. The critical Reynolds numbers obtained from the calculations using the theoretical wavenumbers, however, are quite reasonable.

The streamline plots show that the assumption of axisymmetric disturbances results in a cell pattern not in complete physical agreement with the cell pattern determined from the experimental observations of I. A calculated cell first appears singly within an axial distance of one wavelength. Then the cell develops into two adjacent counter-rotating cells with one cell close to the inner cylinder wall and the other cell near the outer cylinder wall. Subsequently, the two cells become one. This pattern repeats in time; apparently, it is the cause of the oscillations in the perturbation kinetic energy.

The National Science Foundation is gratefully acknowledged for financial support under Grant GK-14275.

REFERENCES

Chen, C. F. & Kirchner, R. P. 1971 Stability of time-dependent rotational Couette flow. Part. 2. Stability analysis. *J. Fluid Mech.* **48**, 365.

Harris, D. L. & Reid, W. D. 1964 On the stability of viscous flow between rotating cylinders. Part 2. Numerical analysis. *J. Fluid Mech.* **20**, 95.

Keller, H. B. 1968 *Numerical Methods for Two-point Boundary-Value Problems.* Waltham, Massachusetts: Blaisdell.

Krueger, E. R., Gross, A. & DiPrima, R. C. 1966 On the relative importance of Taylor-vortex and non-axisymmetric modes in flow between rotating cylinders. *J. Fluid Mech.* **24**, 521.

Liu, D. C. & Chen, C. F. 1973 Numerical experiments on time-dependent rotational Couette flow. *J. Fluid Mech.* **59**, 77.

SNYDER, H. A. 1968 Stability of rotating Couette flow. II. Comparison with numerical results. *Phys. Fluids*, **11**, 1599.

SPARROW, E. M., MUNRO, W. D. & JONSSON, V. K. 1964 Instability of the flow between rotating cylinders: the wide-gap problem. *J. Fluid Mech.* **20**, 35.

WALOWIT, J., TSAO, S. & DIPRIMA, R. C. 1964 Stability of flow between arbitrarily spaced concentric cylindrical surfaces including the effect of a radial temperature gradient. *J. Appl. Mech.* **31**, 585.

WITHJACK, E. M. & CHEN, C. F. 1974 An experimental study of Couette instability of stratified fluids. *J. Fluid Mech.* **66**, 725.